universe

MDPI

Article

Oscillating Magnetized Color Superconducting Quark Stars

Marcos Osvaldo Celi [1,2,*], Mauro Mariani [1,2], Milva Gabriela Orsaria [1,2] and Lucas Tonetto [3,4]

[1] Grupo de Gravitación, Astrofísica y Cosmología, Facultad de Ciencias Astronómicas y Geofísicas, Universidad Nacional de La Plata, Paseo del Bosque S/N, La Plata 1900, Argentina; mmariani@fcaglp.unlp.edu.ar (M.M.); morsaria@fcaglp.unlp.edu.ar (M.G.O.)
[2] Consejo Nacional de Investigaciones Científicas y Técnicas, Godoy Cruz 2290, Ciudad Autónoma de Buenos Aires 1425, Argentina
[3] Dipartimento di Fisica, "Sapienza" University of Rome, Piazzale A. Moro, 5, 00185 Roma, Italy; lucas.tonetto@roma1.infn.it
[4] Istituto Nazionale di Fisica Nucleare, Sezione di Roma, Piazzale A. Moro, 5, 00185 Roma, Italy
* Correspondence: mceli@fcaglp.unlp.edu.ar

Abstract: The main objective of this work is to study the structure, composition, and oscillation modes of color superconducting quark stars with intense magnetic fields. We adopted the MIT bag model within the color superconductivity CFL framework, and we included the effects of strong magnetic fields to construct the equation of state of stable quark matter. We calculated observable quantities, such as the mass, radius, frequency, and damping time of the oscillation fundamental f mode of quark stars, taking into account current astrophysical constraints. The results obtained show that color superconducting magnetized quark stars satisfy the constraints imposed by the observations of massive pulsars and gravitational wave events. Furthermore, the quantities associated with the oscillation f mode of these objects fit the universal relationships for compact objects. In the context of the new multi-messenger gravitational wave astronomy era and the future asteroseismology of neutron stars, we hope that our results contribute to the understanding of the behavior of dense matter and compact objects.

Keywords: neutron stars; quark stars; color superconductivity; di-quarks; magnetic field; oscillations (including pulsations); equation of state; dense matter

Citation: Celi, M.O.; Mariani, M.; Orsaria, M.G.; Tonetto, L. Oscillating Magnetized Color Superconducting Quark Stars. *Universe* **2022**, *8*, 272. https://doi.org/10.3390/universe8050272

Academic Editor: Nicolas Chamel

Received: 29 March 2022
Accepted: 4 May 2022
Published: 6 May 2022

1. Introduction

Strange matter, the possibility that the fundamental state of matter at high densities is a system of quarks in equilibrium against weak interactions, has been the subject of research in a wide variety of scenarios [1–7]. Probably one of the most favorable situations for the appearance of this type of matter, even without being absolutely stable, occurs during the last stages of the evolution of massive stars, associated with the explosion of type II supernovae, and during the formation of neutron stars (NSs) [8–12]. The latter are the densest objects in the universe, with radii of just over a dozen kilometers and masses of around $1.4M_{\odot}$. NSs, in addition to having high densities, have magnetic fields (MFs) from 10^8 up to 10^{15} Gauss at their surface; in particular, the objects with the greatest MF values, $\sim 10^{14-15}$ Gauss, are the so-called magnetars. Under these extreme conditions, QCD predicts that hadronic matter may undergo a transition to a strange matter phase or a color superconducting phase [13]. This prediction, together with the stability of the strange matter hypothesis, opens up the possibility of the formation of compact objects composed entirely of quark matter: quark stars (QSs). The theoretical existence of such compact objects raises questions about what the true composition of NSs is, how astrophysical objects containing strange matter can be detected, and what are the main observational characteristics that differentiate them from objects made of non-strange matter.

During the last decade, some NSs of $2M_{\odot}$ were detected, establishing new restrictions to the equation of state (EoS) of the matter that composes these objects and that is still

unknown. The J1614-2230 pulsar is, among the most massive pulsars observed, the one with the least uncertainty in the determination of its mass, being $M = 1.906 \pm 0.016 M_\odot$ [14–16]. Two other pulsars with a mass greater than two solar masses are J0348+0432, with a mass $M = 2.01 \pm 0.04 M_\odot$ [17], and J0740+6620, with a mass $M = 2.08 \pm 0.07 M_\odot$ [18]. Added to these data are those of the NICER telescope, from which not only the radius of the pulsar J0740+6620 was established, but also the mass and radius of the isolated pulsar J0030+0451 [19,20].

On the other hand, the event called GW170817 corresponds to the detection of the first merger of two NSs, carried out by the LIGO/Virgo collaboration [21], which promoted the era of multi-messenger astronomy with gravitational waves (GWs). This is one of the most promising scenarios to understand the behavior of the dense matter EoS. The analysis of the data from this event allowed for constraints on the mass, radius, and tidal deformability of the merging NSs. On 25 April 2019, a new merger of two NSs, GW190425, was detected, in which more massive NSs participated [22]. The most recent event reported by the LIGO/Virgo collaboration, GW190814, was detected from a binary merger of a black hole and a 2.50–2.67$M_\odot$ compact object, which could be the most massive NS or the least massive black hole ever observed [23]. It is expected that future GW detectors, such as the Einstein Telescope, could detect not only NSs mergers but the emission from the non-radial pulsation modes of isolated NSs; in this context, it is also expected that the fundamental f mode channels most of the GW emission energy [24].

Due the uncertainty of the EoS of matter under extreme conditions of pressure and density and the constraints on NSs from multi-messenger astronomy, we propose that theoretical magnetized color superconducting QSs may shed some light on these questions. At this point, we must emphasize that we study magnetized color superconducting QSs under the assumption of the strange matter hypothesis. This is important because for the first time, a functional dependent magnetic field and the possibility of di-quark formation are both taken into account to study oscillating self-bound stars. Previous works used a uniform and constant MF to study magnetized strange quark matter within a confining model [25] and to study magnetized CFL stars in the framework of the MIT bag and NJL models [26,27]. In particular, the NJL model does not satisfy the strange matter hypothesis [28]. In fact, Paulucci et al. [27] relies on the MIT model analysis by adopting an effective bag by hand in the NJL to construct self-bound stars. Thinking that quark stars are possible, one of the problems with more realistic models to describe quark matter (see for example [29] and the references therein) is the lack of free parameters to adjust them to astrophysical observations. In general, the parameters in this type of model are fixed, relying on vacuum fits, which might not be applicable at the large densities found in compact objects. An alternative model to study self-bound stars that has recently been revisited is the density-dependent quark mass model [30]. For simplicity, we adopted the traditional MIT bag model [31] in our study. This allows us to fit the chosen free parameters not only to the latest astrophysical constraints for compact objects, but also to be consistent when modeling bare self-bound QSs (without a surface crust layer [32]). Details of the construction of such objects and the results for the QSs' EoS, structure, and oscillation f mode will be given in the next sections.

The paper is organized as follows. In Section 2.1, we explain the incorporation of the MF within the MIT bag model. Section 2.2 is devoted to a brief description of the color superconducting phase considered and to show the stability window of stable magnetized color superconducting matter, given the complete modeled EoS. Different families of compact objects, as well as the fundamental f non-radial oscillation frequency and the corresponding damping times obtained are presented in Section 3. In Section 4, we present a summary and discussion of our work.

2. Superconducting Magnetized Strange Quark Matter Equation of State

2.1. Magnetized Strange Quark Matter within the MIT Bag Model

In the presence of an MF, the transverse component of the momentum of a charged particle is quantized into *Landau levels*. Assuming a local z-direction of the MF, this momentum reads [33]:

$$k_\perp^2(\nu) = 2\nu|q|B\,, \tag{1}$$

where q is the electric charge of the particle, B the strength of the MF, and ν a quantum number given by:

$$\nu = n + \frac{1}{2} - \mathrm{sgn}(q)\frac{g}{2}\frac{s}{2}\,, \tag{2}$$

where n is the Landau quantum number, $\mathrm{sgn}(x)$ is the sign function, g is the g-factor, and s is the spin projection of the particle. We consider $g = 2$ for spin $1/2$ particles.

The Landau quantization produces a energy spectrum that is

$$E = \sqrt{k_z^2 + \bar{m}^2(\nu)}\,, \tag{3}$$

with

$$\bar{m}^2(\nu) = m^2 + k_\perp(\nu)^2\,. \tag{4}$$

In order to keep k_z real-valued,

$$k_z(\nu) = \sqrt{E^2 - \bar{m}^2(\nu)}\,, \tag{5}$$

we have to impose the constraint $\nu \leq \nu_{max}$ where,

$$\nu_{\max} = \left\lfloor \frac{E^2 - m^2}{2|q|B} \right\rfloor, \tag{6}$$

and $\lfloor x \rfloor$ is the largest integer less than or equal to x.

The anisotropy of the MF and, consequently, of the momentum components induces an energy–momentum tensor for the matter component given by:

$$T_{\mu\nu}^{\mathrm{matter}} = \mathrm{diag}(\varepsilon, P_\perp, P_\perp, P_\parallel)\,, \tag{7}$$

where ε is the energy density, and the pressure components read

$$\begin{aligned} P_\parallel &= -\Omega\,, \\ P_\perp &= -\Omega - \mathcal{M}B\,, \end{aligned}$$

$\mathcal{M}$ being the matter magnetization [5,34]:

$$\mathcal{M} = -\partial\Omega/\partial B|_{\mu_B}\,. \tag{8}$$

Besides, the pure contribution from the MF generates another anisotropy in the system:

$$T_{\mu\nu}^{\mathrm{MF}} = \mathrm{diag}(B^2/2, B^2/2, B^2/2, -B^2/2)\,. \tag{9}$$

In addition, in the *MIT bag model*, there appears a constant contribution to the energy density and the pressure, which mimics the confinement property of QCD [31,35]. This contribution is treated as a free parameter of the model, Bag, and is given by

$$T_{\mu\nu}^{Bag} = \mathrm{diag}(Bag, -Bag, -Bag, -Bag)\,. \tag{10}$$

Hence, the total energy–momentum tensor of the system turns out to be

$$T_{\mu\nu} = T_{\mu\nu}^{\text{matter}} + T_{\mu\nu}^{Bag} + T_{\mu\nu}^{\text{MF}}\,. \tag{11}$$

As we already have stated in previous works [36,37] and following the work by Strickland et al. [38], in a quark matter system under a locally constant MF in the z-direction, the integrals of thermodynamic quantities are substituted by sums over the transverse momentum due to the quantization. Thus, the particle number density, energy density, and pressures of each i-particle of the system are given by

$$\begin{aligned}
n^i &= \frac{\gamma_c |q| B}{2\pi^2} \sum_{-s}^{+s} \sum_{n=0}^{\nu \leq \nu_{\max}} k_{z,F}\,, \\
\varepsilon^i &= \frac{\gamma_c |q| B}{4\pi^2} \sum_{-s}^{+s} \sum_{n=0}^{\nu \leq \nu_{\max}} \left[E_{\text{F}} k_{z,F} + \bar{m}^2 \ln\left(\frac{E_{\text{F}} + k_{z,F}}{\bar{m}} \right) \right], \\
P_{\parallel}^i &= \frac{\gamma_c |q| B}{4\pi^2} \sum_{-s}^{+s} \sum_{n=0}^{\nu \leq \nu_{\max}} \left[E_{\text{F}} k_{z,F} - \bar{m}^2 \ln\left(\frac{E_{\text{F}} + k_{z,F}}{\bar{m}} \right) \right], \\
P_{\perp}^i &= \frac{\gamma_c |q|^2 B^2}{2\pi^2} \sum_{-s}^{+s} \sum_{n=0}^{\nu \leq \nu_{\max}} \nu \ln\left(\frac{E_{\text{F}} + k_{z,F}}{\bar{m}} \right),
\end{aligned} \tag{12}$$

with $E_F = \mu_i$ (μ_i being the chemical potential of the particle) and $k_{z,F}$ being the Fermi energy and z-momentum, respectively. The factor $\gamma_c = 3$ indicates the degeneracy color number of the quarks.

The determination of the MF direction and strength inside NSs is a very complex problem, which implies the resolution of the non-linear general relativistic magneto-hydrodynamic equations [39]. Magneto-hydrodynamics models have shown that, during the proto-NS stage, the differential rotation would develop high toroidal MF components inside the star [40–42], so both the poloidal and toroidal MF components are necessary to preserve the star stability [43]. Thus, realistic stable models of magnetized NSs require the simultaneous presence of poloidal and toroidal MF components [44–46]. Besides, purely toroidal MFs make the NS prolate, while purely poloidal MFs tend to make it oblate; if both toroidal and poloidal components are of the same order, we may expect that oblateness and prolateness cancel out approximately, leading to stars close to spherical symmetry. In this scenario, known as the *chaotic MF* approximation [47,48], a spatial average can be performed and the spherical symmetry of the total system remains unchanged. Consequently, we can define an effective isotropic pressure given by [36,49,50]:

$$P = \frac{T_{11} + T_{22} + T_{33}}{3} = \sum_{i=u,d,s} \frac{2P_{\perp}^i + P_{\parallel}^i}{3} - Bag + \frac{B^2}{6}\,. \tag{13}$$

Furthermore, when aiming to study the structure and composition of magnetized compact objects, it is usual to avoid the complex MF dynamics and distribution using a functional form to model the MF strength profile in a given direction. Dexheimer et al. [51] used a polynomial MF profile in the star's polar direction, satisfying Maxwell's equations. A polynomial poloidal MF profile in magnetars has also been suggested by Chatterjee et al. [52]. These MF parametrizations are constructed consistently since they satisfy the Maxwell equations, and so, they provide a suitable physics insight into the MF profile inside NSs. However, the accuracy of these profiles in a direction other than polar and their compatibility with the presence of a non-negligible toroidal component have not yet been studied. Furthermore, these profiles are almost flat, and considering a surface value of $B \sim 10^{15}$ Gauss—corresponding to the observed MF surface values for magnetars—they do not allow reaching internal MF strength values much beyond this order of magnitude. This feature prevents reaching MFs of $\sim 10^{17}$–10^{18} Gauss in the center of magnetars, values that emerge from magneto-hydrodynamics simulations [39,41,42,53]; in particular, some

works even suggest that the central MF in hybrid stars with quark matter in their cores could be as large as 10^{19} Gauss [54] and in QSs could be as large as 10^{20} Gauss [55–57].

In this work, we adopted a hypothetical functional form of the MF parametrization depending on the baryonic chemical potential, μ_B, given by

$$B(\mu_B) = B_{min} + B_{max}\left(1 - e^{(\beta((\mu_B - m_n)^\alpha)/m_n)}\right), \tag{14}$$

with $\alpha = 2.5$ and $\beta = -4.08 \times 10^{-4}$ and m_n is the nucleon mass [58]. The parameters $B_{\rm min}$ and $B_{\rm max}$ correspond to the order of magnitude of the MF at the surface and the center of the star, respectively. We define two sets for these parameters to analyze two paradigmatic NS scenarios: the *low MF* pulsar and the *magnetar* (see the details in Table 1). As can be seen in that table, in order to study a wide range of MF values, we selected the value of $B_{max} \lesssim 3 \times 10^{18}$ Gauss according to the constraint imposed by Lai and Shapiro [59], who found that greater MF values could destabilize the star.

The exponential profile of Equation (14), although not physically consistent, is a suitable choice to study bulk properties such as the structure and composition of these compact objects since it allows covering a wide range of MF values. Although hypothetical, this exponential parametrization has been used in several works and is an acceptable approximation to model the complex and still unknown profile of the MF [37,48,58,60–63].

Table 1. MF parametrization values for the two selected astrophysical scenarios: *low-MF* pulsar and *magnetar*.

Scenario	$B_{\rm min}$ (Gauss)	$B_{\rm max}$ (Gauss)
Low-MF	1×10^{13}	1×10^{15}
Magnetar	1×10^{15}	3×10^{18}

2.2. Color Superconductivity and Stability Window

According to the QCD phase diagram, it is likely that, at high densities and low temperatures, strange matter becomes a color superconductor (see for example [64–66]). Any attractive quark–quark interaction in this type of regime would lead to the appearance of condensates called di-quarks, similar to electron condensates in ordinary superconductivity [67]. Thus, conventionally, di-quarks are zero momentum spineless Cooper pairs.

In electromagnetic superconductivity, if the MF applied to the system is greater than a critical value, B_c, Cooper pairs could break and the system is reverted to a normally conducting state. This happens because the electrons in the Cooper pair have equal charges and opposite spins; thus, they have anti-parallel magnetic moments to the MF. The MF will tend to align the two parallel magnetic moments closest to each other, destroying the superconducting state. This transition from the superconducting to the normal state depends on whether the superconductor is of first or second order. In the first-order superconductor, the superconducting state has an abrupt transition to the normal state when $B > B_c$. This type of superconductor is characterized by completely expelling the magnetic field, which is known as the Meissner effect. Second-order superconductors have two critical fields, B_{c1} and B_{c2}; for $B < B_{c1}$, the superconducting state holds, and for $B > B_{c2}$, there exists the normal state. Between B_{c1} and B_{c2}, there is a mixed state in which the flux tubes of the MF may penetrate the superconductor [68]. In the case of color superconductivity, quarks forming di-quarks have opposite charges and spins. Thus, the magnetic moments are parallel to the MF, and therefore, its presence reinforces the color superconductivity [69].

In NSs, superconductivity may be accompanied by the baryon superfluidity and/or the electromagnetic Meissner effect [70], and the MF can be expelled during a long time period [71] or may exist in vortices [72]. In the case of pairing in P-wave states, the superfluidity/superconductivity may remain for $B > B_{c2}$, as in ferromagnetic superconductors and in some color superconducting phases [73].

The analysis of the pairing properties for strange matter as a color superconductor is not trivial due to the variety of flavors, colors, and quark masses involved. In addition, the formation of a color superconducting phase breaks the $SU(3)_c$ color symmetry, so di-quarks are not colorless. Therefore, in the framework of QSs, it will not only be necessary to guarantee the electric charge neutrality, but also the color charge neutrality.

One of the most-studied color superconducting phases is *color flavor locked* (CFL) [13], and it has also been studied considering the presence of an MF [74,75]. This state is a symmetric phase of matter in which all the light quarks, each with three colors, are involved in the pairing process. A schematic representation of the pairing patterns in this phase is shown in Figure 1. The formation of di-quarks lowers the energy of the system by an amount related to the so-called color superconducting gap, Δ. This quantity is a function of the chemical potential, but can be treated as a free parameter of the model. To include the effect of color superconductivity in a phenomenological way, we considered a fictional condition of unpaired quark matter that is in a superconducting state once the quarks involved in the pairing reach a common Fermi momentum (see, for example, Curin et al. [76] and the references therein). The energy of the system is affected by the term

$$\varepsilon_\Delta = -3\left(\frac{\Delta\bar{\mu}}{\pi}\right)^2, \tag{15}$$

where

$$\bar{\mu} = \frac{1}{N}\sum_i \mu_i, \tag{16}$$

is the mean chemical potential related to the N quarks forming di-quarks. The quark chemical potentials considering electric and color charges are given by

$$\mu_i = \mu_B - Q\mu_e + T_3\mu_3 + T_8\mu_8\,, \tag{17}$$

where

$$\begin{aligned} Q &= \mathrm{diag}(2/3, -1/3, -1/3)\,, \\ T_3 &= \mathrm{diag}(1/2, -1/2, 0)\,, \\ T_8 &= \mathrm{diag}(1/3, 1/3, -2/3)\,. \end{aligned}$$

Q is the diagonal matrix corresponding to the electric charge. The color potentials μ_3 and μ_8 are associated with the two color charges of the group $SU(3)_c$ that commute with each other, and T_3 and T_8 are the color charge diagonal matrices, the generators of $SU(3)_c$.

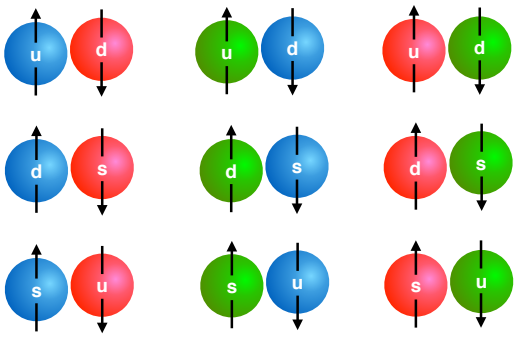

Figure 1. Schematic illustration of the different pairing combinations in the CFL phase. Quarks forming Cooper pairs have opposite charges and spins, and the presence of an MF reinforces the pairing (see text).

Using the Euler relation, the complete EoS of magnetized color superconducting quark matter is given by

$$\varepsilon = -(P - \varepsilon_\Delta) + \sum_{i=u,d,s,e,\mu} \mu_i n^i, \tag{18}$$

where P is given by Equation (13), and the number densities n^i of Equation (12) are modified by the di-quark formation fulfilling the following relationship:

$$n^u = n^d = n^s = n_B\,. \tag{19}$$

where, now, $n^i = \partial(P - \varepsilon_\Delta)/\partial\mu_i$ and n_B is the baryonic number density of the system. Equation (19) is a consequence of imposing both color and electric charge neutrality, the latter given by

$$2n^u - n^d - n^s = 3(n^e + n^\mu)\,. \tag{20}$$

It is important to mention that the CFL phase can undergo stresses due to the mass of the strange quark and the conditions of charge neutrality and beta equilibrium. Furthermore, for this superconducting phase to exist, the pairing between the quarks must be strong enough, i.e., $\Delta > m_s^2/2\mu$, becoming unstable in the limit where $\Delta \sim m_s^2/2\mu$. In particular, *gapless* CFL (gCFL) replaces the CFL phase at $m_s^2/2\mu > \Delta$ [13,77,78]. We obtained that for the two extreme values of the superconducting gap considered, Δ = 10, 90 MeV, the transition from CFL to gCFL should occur for chemical potentials lower than μ = 460.8, 51.2 MeV, respectively, well below the chemical potential values from which the EoSs of Table 2 are physical, that is when the pressure increases monotonically with the energy density. In more realistic quark models, such as NJL, the gCFL phase may have astrophysical implications, controlling the cooling of a neutron star if quark matter in this phase is present [79].

Table 2. Parameters for the four chosen EoSs. All the sets satisfy the strange matter stability hypothesis and the mass constraint $M_{\max} \geq 2.01 M_\odot$. We also show the surface baryonic density, n_B^{sur}, and the central MF strength, B_{cen}, for each set.

EoS #	Δ [MeV]	Bag [MeV/fm^3]	$\varepsilon/n_B\vert_{P=0}$ [MeV]	$M_{\max}$ [$M_\odot$]	n_B^{sur} [1/fm^3]	B_{cen} [10^{18} Gauss]
1	10	45	801.9	2.17	0.23	1.4
2	50	50	794.8	2.18	0.24	1.4
3	90	45	712.0	2.60	0.21	0.6
4	90	70	809.9	2.03	0.30	1.7

For QSs to exist, strange quark matter composing them must fulfill the absolute stability hypothesis. Therefore, to obtain the corresponding stability window, we calculated the energy per baryon of superconducting magnetized quark matter, ε/n_B, at pressure $P = 0$, which corresponds to the conditions on the QSs surface. Due to the observational constraints imposed for NSs with low MFs, we used a constant MF, $B = 10^{12}$ Gauss, for the stability analysis. Hence, once we have built the superconducting magnetized quark EoS, firstly, we will study the stability of quark strange matter within our model. In Figure 2, we present the energy density per baryon as a function of the free parameters of the model: the *Bag* constant and the superconducting gap Δ. Through this analysis, we can find the stability window of our model, which in the figure corresponds to the region below the white curve (the ^{56}Fe mass). As can be seen, we obtain stable strange quark matter for any value of Δ as long as we keep the value of *Bag* low enough.

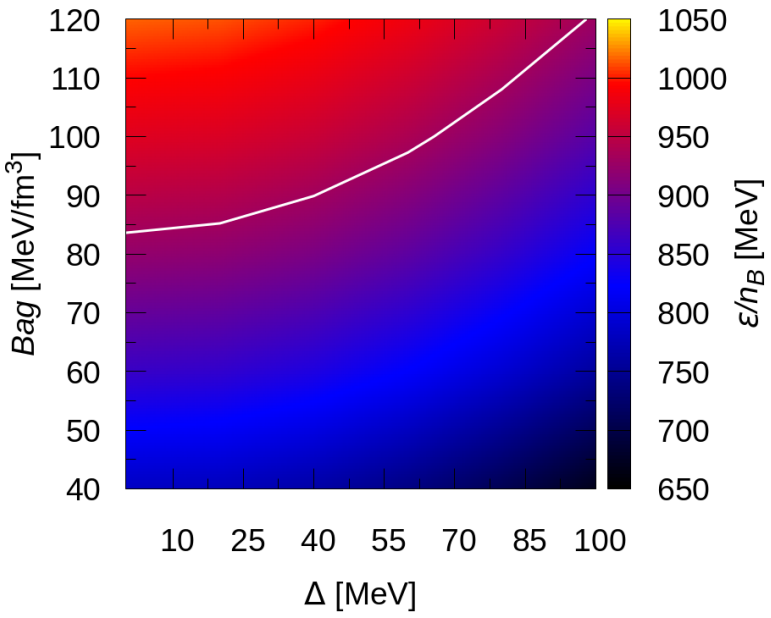

Figure 2. Energy per baryon, ε/n_B, as a color map in the *Bag*–Δ plane considering a low and constant MF, $B = 10^{12}$ Gauss. The white curve indicates the constraint corresponding to the mass of ^{56}Fe. Only *Bag*–Δ pairs below the white curves lead to stable configurations.

3. Solutions of the Structure Equations and f Oscillation Mode

To calculate the structure of color superconducting magnetized QSs, we assumed that these objects have spherical symmetry and do not rotate. Under this hypothesis, it is valid to integrate the well-known relativistic hydrostatic equilibrium equations of Tolman, Oppenheimer, and Volkov (TOV) and obtain several stellar properties for different equations of state. Furthermore, since isolated compact objects can oscillate, we calculated the oscillation frequencies and the associated damping times of their non-radial oscillation modes, because these types of modes emit GWs. We only focused on the fundamental f mode, since it concentrates the largest amount of potentially detectable energy.

In addition to satisfying the stability hypothesis, the QS families obtained with the superconducting magnetized quark EoSs must fulfill the $2.01M_\odot$ constraint imposed by the observation of the pulsar J0740+6620 [16,18]. In Figure 3, we present the QS maximum mass (for a low-MF parametrization; see Table 1) as a function of the *Bag* and Δ parameters, and the white curve represents the $M_{\rm max} = 2.01M_\odot$ restriction. Any combination (*Bag*, Δ) below this curve satisfies such a constraint.

In Figure 4, we show the combination of both the stability window of magnetized superconducting quark matter and the constraint of massive pulsars, Figures 2 and 3, respectively. We selected four sets of parameters, indicated with black numbered dots (see Table 2 for details), from the overlapped region. The choice of sets also allow us to study the effects of *Bag* and Δ parameters in a decoupled way: Sets 1 and 3 (Sets 3 and 4) share the same value of *Bag* (Δ).

Through the selected sets of Table 2, we studied the structure and oscillation f mode of the QSs considering the two MF parametrizations presented in Table 1: low-MF QSs and magnetars. In all results presented hereafter, the continuous (dashed) curves represent stable solutions for low-MF QSs (magnetars). In Figure 5, we present the mass–radius relationship obtained by integrating TOV equations and the constraints in mass and radius imposed by recent observations: the $\sim 2M_\odot$ [16,18] pulsars, GW170817 [21] and GW190425 [22], and NICER observations [19,20,80,81]. It is important to mention that Set 4 does not satisfy the restriction imposed by the pulsar J0030+0451. However, we kept Set 4 in order to perform a comparative analysis with the other chosen parameter sets.

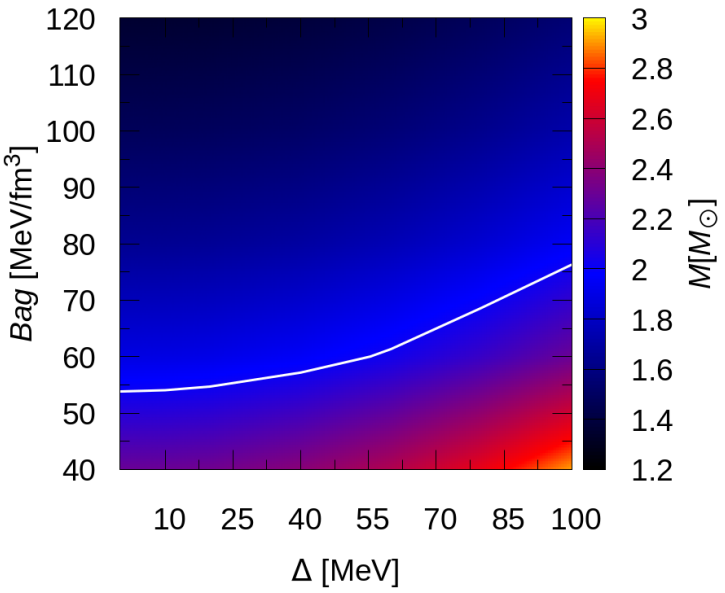

Figure 3. Maximum mass for each QS family, $M_{\max}$, in the *Bag*–Δ plane considering the low MF parametrization. The white curve indicates the constraint of massive pulsars, $M_{\max} = 2.01 M_\odot$.

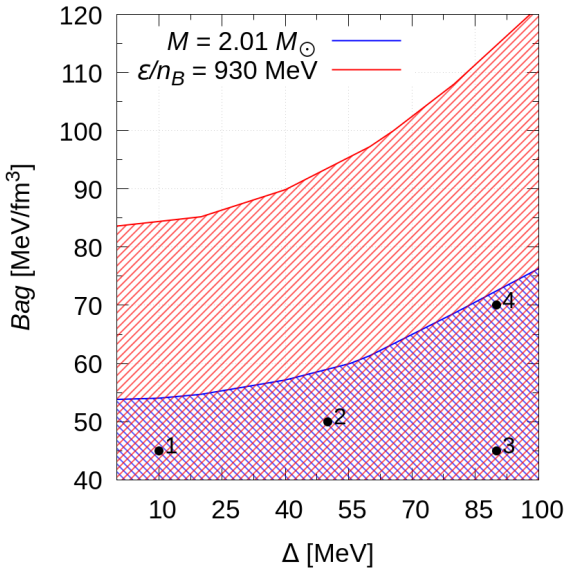

Figure 4. *Bag*–Δ plane showing the stability window and the $M_{\max} \geq 2.01 M_\odot$ allowed regions. We selected four qualitatively representative sets (Table 2) of the general behavior of our model from the overlapping region where both conditions are satisfied.

It can be seen in Figure 5 that the Set 3 curve reaches a maximum mass of $M_{\max} \approx 2.6 M_\odot$, while the other three EoSs have maximum mass values $M_{\max} < 2.2 M_\odot$ (see Table 2); this result can be explained since, given a fixed *Bag*, an increase in Δ produces a *stiffer* EoS (and a higher maximum mass); inversely, given a fixed Δ, an increase in *Bag* produces a *softer* EoS (and a lower maximum mass). This combined effect for Set 3 (corresponding to the highest Δ and lowest *Bag*) leads to the highest maximum mass.

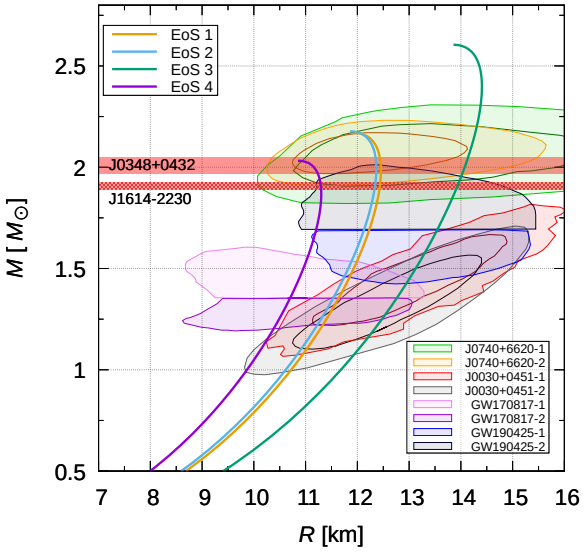

Figure 5. Mass–radius relationships for the sets of Table 2. Continuous curves represent low-MF QSs, and dotted curves represent magnetars. Due to the insignificant effects of the MF on the QS structure, the two scenarios are indistinguishable (see the enlarged details in Figure 6). We also present astrophysical constraints from the $\sim 2\ M_\odot$ pulsars [16,18], the GW170817 [21] and GW190425 [22] events, and NICER observations [19,20,80,81].

Furthermore, the effect of the MF is negligible, and this becomes noticeable in the enlarged Figure 6. This figure shows the detail of continuous and dashed curves around the $M_{\max}$ region in the mass–radius plane. We only show the results for Sets 1 and 4, since for Sets 2 and 3, the differences are smaller; in all cases, the differences are less than 1% in the mass at fixed radius. Furthermore, comparing both Sets 1 and 4, it can be seen that a higher MF does not necessarily imply a higher maximum mass.

On the other hand, to study the oscillation modes of a spherically symmetric body, we must consider not only the oscillations of the star's fluid, but also those that are transferred to space–time through the equations proposed by Detweiler and Lindblom [82]. The Schwarzschild metric [83] being

$$ds^2 = -e^{2\phi(r)}dt^2 + e^{2\lambda(r)}dr^2 + r^2 d\theta^2 + r^2 \operatorname{sen}^2\theta d\phi^2\,, \tag{21}$$

the perturbation functions coupled to the TOV equations are given by [84]

$$\begin{aligned}
H_1' = {} & -r^{-1}\left[l+1+2Me^{\lambda}r^{-1}+4\pi r^2 e^{\lambda}(P-\epsilon)\right]H_1 + r^{-1}e^{\lambda}\left[H_0+K\right. \\
& \left.-16\pi(\epsilon+P)V(r)\right], \\
K' = {} & r^{-1}H_0 + \tfrac{1}{2}l(l+1)r^{-1}H_1 - \left[(l+1)r^{-1} - \tfrac{1}{2}\phi'\right]K - 8\pi(\epsilon+P)e^{\lambda/2}r^{-1}W(r)\,, \\
W' = {} & -(l+1)r^{-1}W(r) + re^{\lambda/2}\left[\gamma^{-1}P^{-1}e^{-\phi/2}X - l(l+1)r^{-2}V(r) + \tfrac{1}{2}H_0 + K\right], \\
X' = {} & -lr^{-1}X + (\epsilon+p)e^{\phi/2}\left\{\tfrac{1}{2}\left(r^{-1} - \tfrac{1}{2}\phi'\right)H_0 + \tfrac{1}{2}\left[r\omega^2 e^{-\phi} + \tfrac{1}{2}l(l+1)r^{-1}\right]H_1\right. \\
& + \tfrac{1}{2}\left(2\phi' - r^{-1}\right)K - \tfrac{1}{2}l(l+1)\phi' r^{-2}V - r^{-1}\left[4\pi(\epsilon+P)e^{\lambda/2} + \omega^2 e^{\lambda/2-\phi}\right. \\
& \left.\left. - \tfrac{1}{2r^2}\left(r^{-2}e^{-\lambda/2}\phi'\right)\right]W\right],
\end{aligned} \tag{22}$$

where H_0, H_1, H_2, and K are time-dependent perturbation functions, γ is the adiabatic factor, and $W(r)$ and $V(r)$ are functions characterizing the fluid perturbation [82]. The numerical resolution of Equation (22) allows us to obtain the oscillation modes of the studied stellar configurations. These modes are known as *quasi-normal modes* (QNMs), since the resulting frequencies are complex, $\omega = 2\pi\nu + i/\tau$, where ν is the real oscillation

frequency and τ is the oscillation damping time of the corresponding mode. As we already stated, we are interested particularly in the solution of the fundamental f mode. As we are only interested in the pressure f mode, the presence of the magnetic restoration force that induces the magnetic Alfvén modes, or any other magnetic contribution, is not relevant in the perturbation equations. Thus, for the pressure modes, only the MF effects on the pressure are relevant, and we introduce them trough the magnetized EoS.

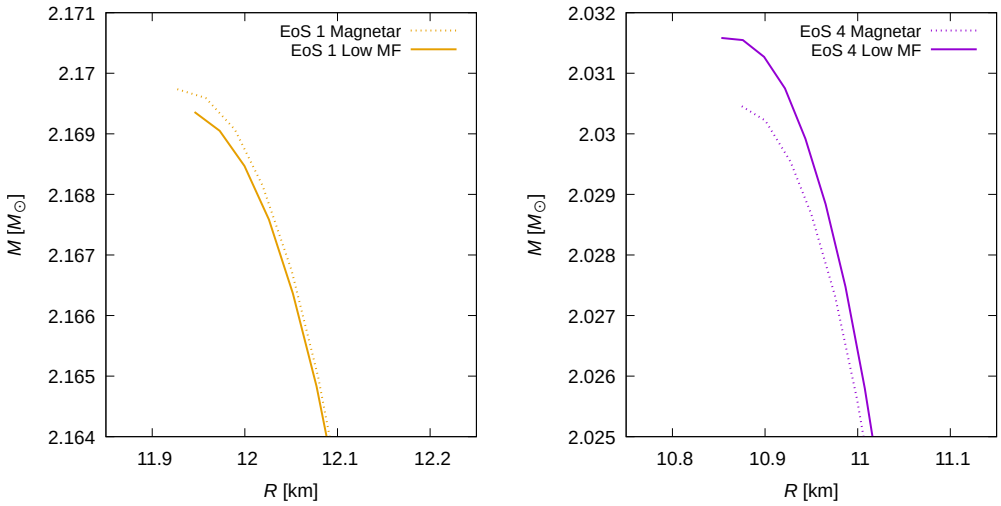

Figure 6. Enlarged zoomed-in view of the mass–radius relationships for the sets of Table 2. Continuous (dotted) curves represent low-MF (magnetars) QSs. It can be seen that the effect of the MF is negligible. Besides, a higher MF does not imply necessarily a higher value for $M_{\max}$. QS families constructed using EoSs 1 and 4 are more sensitive to the variation of the MF strength.

In Figure 7, we present the results for the f mode in the ν-mass (left panel) and τ-mass (right panel) planes. In the ν-mass plane, it can be seen that oscillation frequencies are not only increasing with the mass of the stellar configurations, but also that families of QSs with higher maximum masses have lower oscillation frequencies; e.g., for a QS of $2M_{\odot}$, $\nu \sim 2100$ Hz for Set 4, $M_{\max} \approx 2.03M_{\odot}$ and $M_{\max} \approx 2.17M_{\odot}$ correspond to $\nu \sim 1780$ Hz for Sets 1 and 2, and $M_{\max} \approx 2.6M_{\odot}$ corresponds to $\nu \sim 1450$ Hz for Set 3. Comparing Sets 1 and 3, it follows that an increase in Δ generates lower frequencies; comparing Sets 3 and 4, we observe that an increase in the *Bag* produces an increase in the frequency values. In particular, we also calculated the f mode for the non-superconducting magnetized strange quark matter ($\Delta = \mu_3 = \mu_8 = 0$) with $Bag = 45$ MeV/fm^3. This particular choice allows us to compare the non-superconducting case with Sets 1 and 3. As we have already shown, an increase in Δ implies lower f mode frequencies, and this behavior is also valid in the limit of $\Delta = 0$. For a given *Bag* value, the non-superconducting case has the highest frequency, and the appearance of the superconducting phase implies a decrease in the frequency. To quantify this comparison, we calculated the percentage change for the $M_{\max}$ QS as an indicator of the whole family's results; if we compare the non-superconducting case with those of the $\Delta = 10$ MeV and $\Delta = 90$ MeV results, ν has a shift of $\sim$1% and $\sim$15%, respectively. On the other hand, analogous to what happens in the mass–radius plane, the effect of an intense MF is practically negligible over the values of the f mode oscillation frequencies (see the enlarged Figure 8 for details of Sets 1 and 4).

Considering all the sets, for masses 1.0–2.6$M_{\odot}$, we obtained frequencies in the range 1200–2200 Hz. Previous works obtained qualitatively similar results for purely hadronic, hybrid, or quark stars [48,85–89]; thus, it is not possible to distinguish among hadronic, hybrid, or quark EoSs through the eventual detection of the f mode frequency. In particular, Flores and Lugones [87] studied color superconducting QSs at zero MF and their results are in agreement with those obtained in this work for the frequencies associated with the f mode.

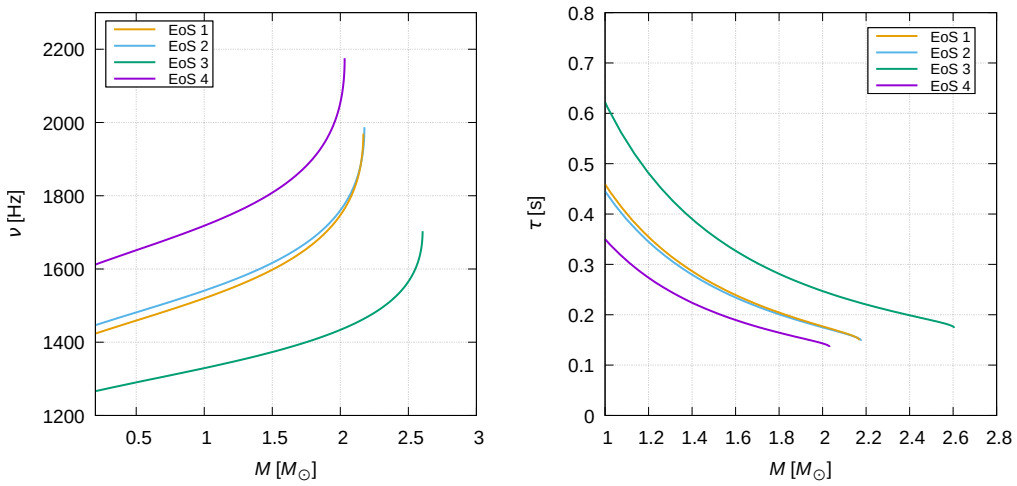

Figure 7. ν–mass (**left** panel) and τ–mass (**right** panel) relationships for the sets of Table 2. Continuous curves represent low-MF QSs, and dotted curves represent magnetars. Due to the negligible effects of the MF on the QS structure, both astrophysical scenarios are indistinguishable (see enlarged Figure 8 for details). It can be seen that the EoS producing the highest maximum mass results in the lowest frequency values and longest damping times.

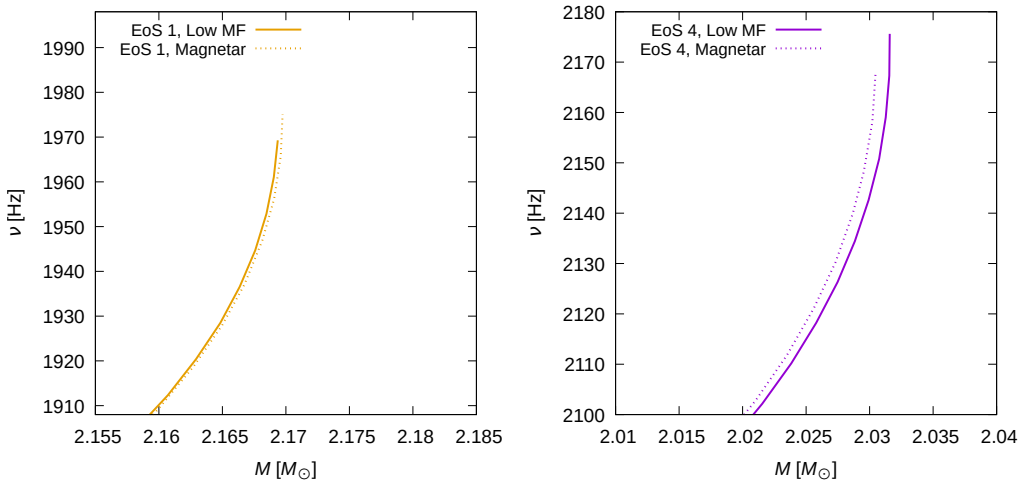

Figure 8. Enlarged zoomed-in view of the frequency–mass relationships for the sets of Table 2. Continuous (dotted) curves represent low-MF (magnetars) QSs. The effect of the MF is negligible; as we already pointed out in the mass–radius relationship, the QS families constructed using EoSs 1 and 4 are more sensitive to the variation of the MF strength.

For the τ–mass relationship, presented in the right panel of Figure 7, our results are in the range of 0.1–0.6 s, also in agreement with the previously mentioned works [48,85–88]. Contrary to the ν behavior, τ decreases with the mass, and the curves of the QS families with a higher maximum mass correspond to higher τ. Besides, an increase in Δ produces increased τ, while an increase in *Bag* causes a reduction in τ. In the non-superconducting case, τ has the lowest value, and it increases when we consider color superconductivity; comparing the non-superconducting result with Sets 1 and 3 for $M_{\rm max}$, τ has a less than 1% shift between the $\Delta = 0$ and $\Delta = 10$ MeV cases and a $\sim 17\%$ shift between the $\Delta = 0$ and $\Delta = 90$ MeV cases. The effect of the MF strength is negligible.

On the other hand, there exist *universal relationships* associated with the oscillation frequencies and damping times for the f mode [90]. In particular, there are empirical

relations relating the frequency and damping time to the mass and radius of a stellar object given by

$$\nu = a_1 + b_1 \sqrt{\frac{M}{R^3}}\,, \tag{23}$$

$$\frac{R^4}{M^3\tau} = a_2 + b_2 \sqrt{\frac{M}{R}} + c_2 \frac{M}{R}\,. \tag{24}$$

In order to analyze how the magnetized color superconducting EoS fits the universal relationships, we used two fits in Equations (23) and (24): BFG fit for hadronic matter [91] and CFL fit for quark matter [87] (see Table 3 for details). If the universality of these relationships holds, the detection of both the frequency and damping time of the fundamental mode of a given compact object allows us to infer the properties of the star such as mass and radius, independently of the EoS used to describe its composition. In Figure 9, we present our results and the mentioned fits for the ν (left panel) and τ (right panel) universal relationships. As can be seen, the results for all the sets are grouped in very narrow regions along the CFL fit. The main difference between the EoSs used in this work and the EoSs of [87] is the strange quark mass, m_s. We added a new fit (detailed in the last column of Table 3) corresponding to m_s = 96 MeV, used in Equation (23), which matches very well with all the EoSs of the present work. Flores and Lugones [87] used m_s = 150 MeV. Moreover, they considered zero magnetic field and massless u and d quarks, and they did not take into account the color chemical potentials, μ_3 and μ_8. The difference in the coefficient values between both fits are not significant, indicating the usual dispersion from the universal relationships for different EoS models. Therefore, within our model, the universal relations developed by Andersson and Kokkotas [90] are valid and the results obtained are in agreement with the fit for QSs presented by Flores and Lugones [87].

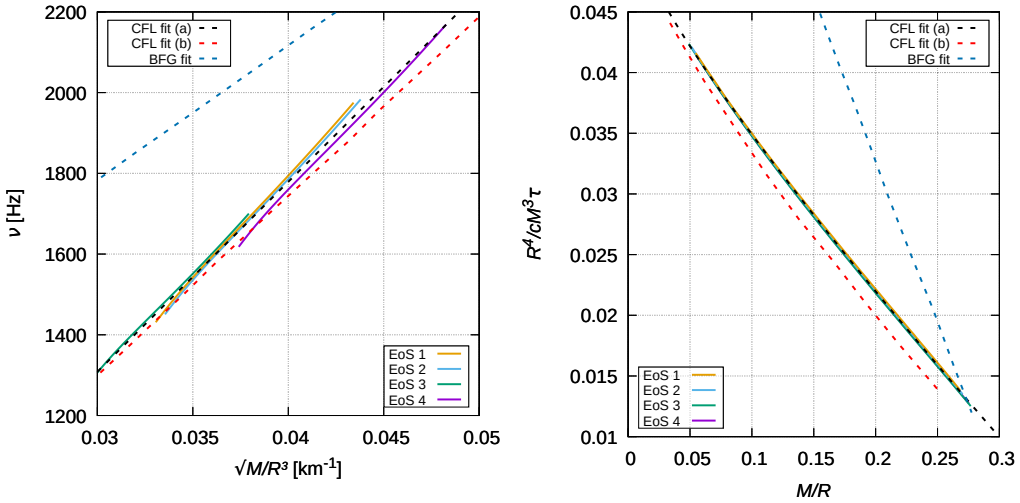

Figure 9. Universal relationships proposed by Andersson and Kokkotas [90] for the f mode, for ν as a function of the mean density (**left** panel) and for τ as a function of the compactness (**right** panel). In both panels, we also show the BFG [91] and two CFL fits; CFL fit (a) corresponds to the fit calculated in this paper and CFL fit (b) to Flores and Lugones' fit [87]. Our fit lies, predictably, close to the CFL fit (b).

Table 3. Parameters for the BFG [91] and CFL [87] fits related to the f mode in Equations (23) and (24). In the third column, we show the parameters fitting our magnetized CFL results.

Fit	a_1 (Hz)	b_1 (km Hz)	a_2	b_2	c_2
BFG	790	33×10^3	8.7×10^{-2}	0	−0.271
CFL [87]	−23	44.11×10^3	0.0553	−0.0466	−0.0725
CFL (this paper)	−103	47.07×10^3	0.0534	−0.0302	−0.0897

4. Summary and Discussion

Using the MIT bag model, including MF and CFL color superconductivity effects, we modeled magnetized color superconducting quark stars and calculated their oscillation f mode and associated frequencies and damping times. For the treatment of the MF, we adopted the chaotic approximation and a functional profile with realistic surface and central MF values for the two astrophysical scenarios considered: low-MF and magnetar QS. We constructed the stability window for magnetized superconducting quark matter and took into account the constraint of massive pulsars to select four sets of parameters that represent the qualitative behavior of the model used. For these four EoSs, we analyzed the mass–radius diagram considering the last constraints on neutron stars given by the GW events 170817 and 190425 and NICER observations. In addition, we verified the universal relations for the frequencies and damping times associated with the oscillation f mode for the chosen EoSs.

The results show that the inclusion of a superconducting color term related to di-quark formation in the EoS produces significant effects, not only on the stability window of strange quark matter, but also on astrophysical quantities, such as the maximum mass, radii, or oscillation f mode of QSs.

On the other hand, the differences of the EoSs in the cases of low and intense MFs are practically negligible. This leads to the fact that the results of mass, radius, and oscillation frequencies obtained do not present differences when comparing both astrophysical scenarios. In particular, for the f mode, our results are in agreement with the work by Lander et al. [92], where, under a Newtonian approach for NSs, they predicted a small shift, proportional to the influence of the pure magnetic pressure, $\propto B^2$, on the total pressure. It is worth mentioning that, if we had used a realistic MF internal distribution, such as the polynomial profiles by Dexheimer et al. [51], Chatterjee et al. [52] or the ones arising from MHD simulations [39], together with the magnetar observed surface value $B \sim 10^{15}$ Gauss, these results would not have changed qualitatively. The fact that the considered quark EoSs only show significant shifts for $B \gtrsim 10^{19}$ Gauss results in that all the discussed parametrizations would have shown negligible MF effects.

Except in the case of EoS 4, the families of stars built with EoSs 1, 2, and 3 satisfy the observational restrictions imposed by GWs, NICER, and massive pulsars. However, EoS 4 is useful to identify the behavior of the *Bag* and Δ parameters compared to the other considered EoSs.

The frequencies and damping times of the QNM f mode are in agreement with the results of purely hadronic, hybrid, and quark stars from previous works [48,85–88]. This implies that if the emission of the f mode could be detected, it would be impossible to distinguish whether these signals come from a purely hadronic, hybrid, or quark star by simply determining the frequency or damping time. We also observed that *stiffened* EoSs, those that provide mass–radius curves with higher maximum masses, give rise to lower oscillation frequencies and higher damping times when compared with *softened* EoSs.

The QNMs obtained fit very well with the universal relationships corresponding to QSs' EoSs. The analysis of these empirical relations would allow not only obtaining structural parameters of the detected object independent of the EoS, such as mass or radius, but also classifying such a compact object and finding possible observational evidence of quark matter in its composition.

It is expected that the third-generation GW observatories, such as the Einstein Telescope, could detect f mode emissions of isolated NSs; we hope that our results can be tested once these detectors start operating in the next few years.

Author Contributions: Conceptualization, M.M.; Data curation, M.O.C.; Formal analysis, M.O.C., M.M., M.G.O. and L.T.; Funding acquisition, M.G.O.; Investigation, M.O.C., M.M. and L.T.; Methodology, M.O.C.; Project administration, M.G.O.; Software, M.O.C., M.M. and L.T.; Supervision, M.M. and M.G.O.; Writing—original draft, M.M. and M.G.O.; Writing—review & editing, M.O.C. and L.T. The authors contributed equally to the theoretical and numerical aspects of the work presented in this paper. All authors have read and agreed to the published version of the manuscript.

Funding: This research was supported by CONICET and UNLP, Grant Numbers PIP 0714 and G 157.

Acknowledgments: The authors thank the anonymous Referees for their corrections and suggestions, which helped improve the quality of the manuscript. M.O.C. and M.M. are fellows of Consejo Nacional de Investigaciones Científicas y Técnicas (CONICET). M.M. and M.G.O. thank CONICET and the Universidad Nacional de La Plata (UNLP) for financial support. L.T. thanks the Italian Istituto Nazionale di Fisica Nucleare (INFN) under Grant TEONGRAV.

Conflicts of Interest: The authors declare no conflict of interest.

References

1. Chakrabarty, S.; Raha, S.; Sinha, B. Strange quark matter and the mechanism of confinement. *Phys. Lett. B* **1989**, *229*, 112–116. [CrossRef]
2. Saito, T.; Hatano, Y.; Fukada, Y.; Oda, H. Is there strange-quark matter in galactic cosmic rays? *Phys. Rev. Lett.* **1990**, *65*, 2094. [CrossRef] [PubMed]
3. Madsen, J. Physics and astrophysics of strange quark matter. In *Hadrons in Dense Matter and Hadrosynthesis*; Springer: Berlin/Heidelberg, Germany, 1999; pp. 162–203.
4. Weber, F. Strange quark matter and compact stars. *Prog. Part. Nucl. Phys.* **2005**, *54*, 193–288. [CrossRef]
5. González Felipe, R.; Pérez Martínez, A.; Pérez Rojas, H.; Orsaria, M. Magnetized strange quark matter and magnetized strange quark stars. *Phys. Rev. C* **2008**, *77*, 015807. [CrossRef]
6. Han, K.; Ashenfelter, J.; Chikanian, A.; Emmet, W.; Finch, L.E.; Heinz, A.; Madsen, J.; Majka, R.; Monreal, B.; Sandweiss, J. Search for stable strange quark matter in Lunar soil. *Phys. Rev. Lett.* **2009**, *103*, 092302. [CrossRef]
7. Paulucci, L.; Horvath, J.E. Strange quark matter fragmentation in astrophysical events. *Phys. Lett. B* **2014**, *733*, 164–168. [CrossRef]
8. Dai, Z.; Peng, Q.; Lu, T. The conversion of two-flavor to three-flavor quark matter in a Supernova core. *Astrophys. J.* **1995**, *440*, 815. [CrossRef]
9. Benvenuto, O.; Lugones, G. The phase transition from nuclear matter to quark matter during proto-neutron star evolution. *Mon. Not. R. Astron. Soc.* **1999**, *304*, L25–L29. [CrossRef]
10. Sagert, I.; Fischer, T.; Hempel, M.; Pagliara, G.; Schaffner-Bielich, J.; Mezzacappa, A.; Thielemann, F.K.; Liebendörfer, M. Signals of the QCD phase transition in core-collapse supernovae. *Phys. Rev. Lett.* **2009**, *102*, 081101. [CrossRef]
11. Bombaci, I.; Logoteta, D.; Providência, C.; Vidana, I. Effects of quark matter nucleation on the evolution of proto-neutron stars. *Astron. Astrophys.* **2011**, *528*, A71. [CrossRef]
12. Malfatti, G.; Orsaria, M.G.; Contrera, G.A.; Weber, F.; Ranea-Sandoval, I.F. Hot quark matter and (proto-) neutron stars. *Phys. Rev. C Nucl. Phys.* **2019**, *100*, 015803. [CrossRef]
13. Alford, M.G.; Schmitt, A.; Rajagopal, K.; Schäfer, T. Color superconductivity in dense quark matter. *Rev. Mod. Phys.* **2008**, *80*, 1455. [CrossRef]
14. Demorest, P.B.; Pennucci, T.; Ransom, S.M.; Roberts, M.S.E.; Hessels, J.W.T. A two-solar-mass neutron star measured using Shapiro delay. *Nature* **2010**, *467*, 1081–1083. [CrossRef] [PubMed]
15. Fonseca, E.; Pennucci, T.T.; Ellis, J.A.; Stairs, I.H.; Nice, D.J.; Ransom, S.M.; Demorest, P.B.; Arzoumanian, Z.; Crowter, K.; Dolch, T.; et al. The NANOGrav Nine-year Data Set: Mass and Geometric Measurements of Binary Millisecond Pulsars. *Astrophys. J.* **2016**, *832*, 167. [CrossRef]
16. Arzoumanian, Z.; Brazier, A.; Burke-Spolaor, S.; Chamberlin, S.; Chatterjee, S.; Christy, B.; Cordes, J.M.; Cornish, N.J.; Crawford, F.; Cromartie, H.T.; et al. The NANOGrav 11-year Data Set: High-precision Timing of 45 Millisecond Pulsars. *Astrophys. J. Suppl. Ser.* **2018**, *235*, 37. [CrossRef]
17. Antoniadis, J.; Freire, P.C.; Wex, N.; Tauris, T.M.; Lynch, R.S.; Van Kerkwijk, M.H.; Kramer, M.; Bassa, C.; Dhillon, V.S.; Driebe, T.; et al. A Massive Pulsar in a Compact Relativistic Binary. *Science* **2013**, *340*, 6131. [CrossRef]
18. Fonseca, E.e.a. Refined Mass and Geometric Measurements of the High-mass PSR J0740+6620. *Astrophys. J. Lett.* **2021**, *915*, L12. [CrossRef]
19. Riley, T.E.; Watts, A.L.; Bogdanov, S.; Ray, P.S.; Ludlam, R.M.; Guillot, S.; Arzoumanian, Z.; Baker, C.L.; Bilous, A.V.; Chakrabarty, D.; et al. A NICER View of PSR J0030+0451: Millisecond Pulsar Parameter Estimation. *Astrophys. J. Lett.* **2019**, *887*, L21. [CrossRef]
20. Miller, M.C.; Lamb, F.K.; Dittmann, A.J.; Bogdanov, S.; Arzoumanian, Z.; Gendreau, K.C.; Guillot, S.; Harding, A.K.; Ho, W.C.G.; Lattimer, J.M.; et al. PSR J0030+0451 Mass and Radius from NICER Data and Implications for the Properties of Neutron Star Matter. *Astrophys. J. Lett.* **2019**, *887*, L24. [CrossRef]
21. Abbott, B.P.; Abbott, R.; Abbott, T.D.; Acernese, F.; Ackley, K.; Adams, C.; Adams, T.; Addesso, P.; Adhikari, R.X.; Adya, V.B.; et al. GW170817: Observation of Gravitational Waves from a Binary Neutron Star Inspiral. *Phys. Rev. Lett.* **2017**, *119*, 161101. [CrossRef]
22. Abbott, B.P.; Abbott, R.; Abbott, T.D.; Abraham, S.; Acernese, F.; Ackley, K.; Adams, C.; Adhikari, R.X.; Adya, V.B.; Affeldt, C.; et al. GW190425: Observation of a Compact Binary Coalescence with Total Mass $\sim 3.4\,M_{\odot}$. *Astrophys. J. Lett.* **2020**, *892*, L3. [CrossRef]
23. Abbott, R.; Abbott, T.; Abraham, S.; Acernese, F.; Ackley, K.; Adams, C.; Adhikari, R.; Adya, V.; Affeldt, C.; Agathos, M.; et al. GW190814: Gravitational waves from the coalescence of a 23 solar mass black hole with a 2.6 solar mass compact object. *Astrophys. J. Lett.* **2020**, *896*, L44. [CrossRef]

24. Morozova, V.; Radice, D.; Burrows, A.; Vartanyan, D. The Gravitational Wave Signal from Core-collapse Supernovae. *Astrophys. J.* **2018**, *861*, 10. [CrossRef]
25. Sinha, M.; Huang, X.G.; Sedrakian, A. Strange quark matter in strong magnetic fields within a confining model. *Phys. Rev. D* **2013**, *88*, 025008. [CrossRef]
26. Pérez Martínez, A.; González Felipe, R.; Manreza Paret, D. Compact Stars and Magnetized Cfl Matter. *Int. J. Mod. Phys. E* **2011**, *20*, 84–92. [CrossRef]
27. Paulucci, L.; Ferrer, E.J.; de La Incera, V.; Horvath, J. Equation of state for the magnetic-color-flavor-locked phase and its implications for compact star models. *Phys. Rev. D* **2011**, *83*, 043009. [CrossRef]
28. Buballa, M. NJL-model analysis of dense quark matter. *Phys. Rep.* **2005**, *407*, 205–376. [CrossRef]
29. Dumm, D.G.; Carlomagno, J.P.; Scoccola, N.N. Strong-Interaction Matter under Extreme Conditions from Chiral Quark Models with Nonlocal Separable Interactions. *Symmetry* **2021**, *13*, 121. [CrossRef]
30. Backes, B.C.; Hafemann, E.; Marzola, I.; Menezes, D.P. Density-dependent quark mass model revisited: Thermodynamic consistency, stability windows and stellar properties. *J. Phys. G Nucl. Part. Phys.* **2021**, *48*, 055104. [CrossRef]
31. Chodos, A.; Jaffe, R.L.; Johnson, K.; Thorn, C.B.; Weisskopf, V.F. New extended model of hadrons. *Phys. Rev. D Part. Fields Gravit. Cosmol.* **1974**, *9*, 3471–3495. [CrossRef]
32. Weber, F.; Orsaria, M.; Rodrigues, H.; Yang, S.H. *Structure of Quark Stars*; Neutron Stars and Pulsars: Challenges and Opportunities after 80 Years; van Leeuwen, J., Ed.; Cambridge University Press: Cambridge, UK, 2013; Volume 291, pp. 61–66. [CrossRef]
33. Landau, L.; Lifshitz, E. *Quantum Mechanics: Non-Relativistic Theory*; Course of Theoretical Physics; Elsevier Science: Amsterdam, The Netherlands, 1981.
34. Blandford, R.D.; Hernquist, L. Magnetic susceptibility of a neutron star crust. *J. Phys. C Solid State Phys.* **1982**, *15*, 6233–6243. https://doi.org/10.1088/0022-3719/15/30/017.
35. Chodos, A.; Jaffe, R.L.; Johnson, K.; Thorn, C.B. Baryon structure in the bag theory. *Phys. Rev. D* **1974**, *10*, 2599–2604. [CrossRef]
36. Mariani, M.; Orsaria, M.G.; Ranea-Sandoval, I.F.; Lugones, G. Magnetized hybrid stars: Effects of slow and rapid phase transitions at the quark-hadron interface. *Mon. Not. R. Astron. Soc.* **2019**, *489*, 4261–4277. [CrossRef]
37. Mariani, M.; Tonetto, L.; Rodríguez, M.C.; Celi, M.O.; Ranea-Sandoval, I.F.; Orsaria, M.G.; Pérez Martínez, A. Oscillating magnetized hybrid stars under the magnifying glass of multimessenger observations. *Mon. Not. R. Astron. Soc.* **2022**, *512*, 517–534. [CrossRef]
38. Strickland, M.; Dexheimer, V.; Menezes, D.P. Bulk properties of a Fermi gas in a magnetic field. *Phys. Rev. D* **2012**, *86*, 125032. [CrossRef]
39. Pili, A.G.; Bucciantini, N.; Del Zanna, L. Axisymmetric equilibrium models for magnetized neutron stars in General Relativity under the Conformally Flat Condition. *Mon. Not. R. Astron. Soc.* **2014**, *439*, 3541–3563. [CrossRef]
40. Bonanno, A.; Rezzolla, L.; Urpin, V. Mean-field dynamo action in protoneutron stars. *Astron. Astrophys.* **2003**, *410*, L33–L36. [CrossRef]
41. Naso, L.; Rezzolla, L.; Bonanno, A.; Paternò, L. Magnetic field amplification in proto-neutron stars. The role of the neutron-finger instability for dynamo excitation. *Astron. Astrophys.* **2008**, *479*, 167–176. [CrossRef]
42. Frieben, J.; Rezzolla, L. Equilibrium models of relativistic stars with a toroidal magnetic field. *Mon. Not. R. Astron. Soc.* **2012**, *427*, 3406–3426. [CrossRef]
43. Ciolfi, R.; Rezzolla, L. Poloidal-field Instability in Magnetized Relativistic Stars. *Astrophys. J.* **2012**, *760*, 1. [CrossRef]
44. Braithwaite, J.; Spruit, H.C. Evolution of the magnetic field in magnetars. *Astron. Astrophys.* **2006**, *450*, 1097–1106. [CrossRef]
45. Ciolfi, R.; Rezzolla, L. Twisted-torus configurations with large toroidal magnetic fields in relativistic stars. *Mon. Not. R. Astron. Soc. Lett.* **2013**, *435*, L43–L47. [CrossRef]
46. Sur, A.; Haskell, B.; Kuhn, E. Magnetic field configurations in neutron stars from MHD simulations. *Mon. Not. R. Astron. Soc.* **2020**, *495*, 1360–1371. [CrossRef]
47. Zel'dovich, Y.; Novikov, I. *Stars and Relativity*; Dover Books on Physics; Dover Publications: Mineola, NY, USA, 2014. [CrossRef]
48. Flores, C.V.; Lopes, L.L.; Castro, L.B.; Menezes, D.P. Gravitational wave signatures of highly magnetized neutron stars. *Eur. Phys. J. C* **2020**, *80*, 1142. https://doi.org/10.1140/epjc/s10052-020-08705-1.
49. Bednarek, I.; Brzezina, A.; Mańka, R.; Zastawny-Kubica, M. The influence of asymmetry on a magnetized proto-neutron star. *Nucl. Phys. A* **2003**, *716*, 245–256. [CrossRef]
50. Flores, C.V.; Castro, L.B.; Lugones, G. Properties of strongly magnetized ultradense matter and its effects on magnetar pulsations. *Phys. Rev. C* **2016**, *94*, 015807. [CrossRef]
51. Dexheimer, V.; Franzon, B.; Gomes, R.; Farias, R.; Avancini, S.; Schramm, S. What is the magnetic field distribution for the equation of state of magnetized neutron stars? *Phys. Lett. B* **2017**, *773*, 487–491. [CrossRef]
52. Chatterjee, D.; Novak, J.; Oertel, M. Magnetic field distribution in magnetars. *Phys. Rev. C* **2019**, *99*, 055811. [CrossRef]
53. Igoshev, A.P.; Popov, S.B.; Hollerbach, R. Evolution of Neutron Star Magnetic Fields. *Universe* **2021**, *7*, 351. [CrossRef]
54. Sotani, H.; Tatsumi, T. Massive hybrid quark stars with strong magnetic field. *Mon. Not. R. Astron. Soc.* **2015**, *447*, 3155–3161. [CrossRef]
55. Ferrer, E.J.; de la Incera, V.; Keith, J.P.; Portillo, I.; Springsteen, P.L. Equation of state of a dense and magnetized fermion system. *Phys. Rev. C* **2010**, *82*, 065802. [CrossRef]

56. Chu, P.C.; Li, X.H.; Ma, H.Y.; Wang, B.; Dong, Y.M.; Zhang, X.M. Quark matter and quark stars in strong magnetic fields at finite temperature within the confined-isospin-density-dependent mass model. *Phys. Lett. B* **2018**, *778*, 447–453. [CrossRef]
57. Chu, P.C.; Zhou, Y.; Jiang, Y.Y.; Ma, H.Y.; Liu, H.; Zhang, X.M.; Li, X.H. Quark star matter in heavy quark stars. *Eur. Phys. J. C* **2021**, *81*, 93. [CrossRef]
58. Dexheimer, V.; Negreiros, R.; Schramm, S. Hybrid stars in a strong magnetic field. *Eur. Phys. J. A* **2012**, *48*, 189. [CrossRef]
59. Lai, D.; Shapiro, S.L. Cold Equation of State in a Strong Magnetic Field: Effects of Inverse beta-Decay. *Astrophys. J.* **1991**, *383*, 745. [CrossRef]
60. Bandyopadhyay, D.; Chakrabarty, S.; Pal, S. Quantizing Magnetic Field and Quark-Hadron Phase Transition in a Neutron Star. *Phys. Rev. Lett.* **1997**, *79*, 2176–2179. [CrossRef]
61. Mao, G.J.; Iwamoto, A.; Li, Z.X. A Study of Neutron Star Structure in Strong Magnetic Fields that includes Anomalous Magnetic Moments. *Chin. J. Astron. Astrophys.* **2003**, *3*, 359–374. [CrossRef]
62. Rabhi, A.; Pais, H.; Panda, P.K.; Providência, C. Quark-hadron phase transition in a neutron star under strong magnetic fields. *J. Phys. G Nucl. Phys.* **2009**, *36*, 115204. [CrossRef]
63. Thapa, V.B.; Sinha, M.; Li, J.J.; Sedrakian, A. Equation of State of Strongly Magnetized Matter with Hyperons and Δ-Resonances. *Particles* **2020**, *3*, 660–675. [CrossRef]
64. Rajagopal, K. Mapping the QCD phase diagram. *Nucl. Phys. A* **1999**, *661*, 150–161. [CrossRef]
65. Fukushima, K.; Hatsuda, T. The phase diagram of dense QCD. *Rep. Prog. Phys.* **2010**, *74*, 014001. [CrossRef]
66. Guenther, J.N. Overview of the QCD phase diagram. *Eur. Phys. J. A* **2021**, *57*, 1–23. [CrossRef]
67. Bardeen, J.; Cooper, L.N.; Schrieffer, J.R. Microscopic Theory of Superconductivity. *Phys. Rev.* **1957**, *106*, 162–164. [CrossRef] [PubMed]
68. Glampedakis, K.; Andersson, N.; Samuelsson, L. Magnetohydrodynamics of superfluid and superconducting neutron star cores. *Mon. Not. R. Astron. Soc.* **2011**, *410*, 805–829. [CrossRef]
69. Ferrer, E.J.; de la Incera, V.; Manuel, C. Colour superconductivity in a strong magnetic field. *J. Phys. Math. Gen.* **2006**, *39*, 6349–6355. [CrossRef]
70. Shovkovy, I.A. Two Lectures on Color Superconductivity. *Found. Phys.* **2005**, *35*, 1309–1358. [CrossRef]
71. Baym, G.; Pethick, C.; Pines, D.; Ruderman, M. Spin up in neutron stars: The future of the Vela pulsar. *Nature* **1969**, *224*, 872–874. [CrossRef]
72. Haskell, B.; Sedrakian, A. Superfluidity and Superconductivity in Neutron Stars. In *The Physics and Astrophysics of Neutron Stars*; Springer International Publishing: New York, NY, USA, 2018; pp. 401–454. [CrossRef]
73. Voskresensky, D.N. Vector-boson condensates, spin-triplet superfluidity of paired neutral and charged fermions, and $3P_2$ pairing of nucleons. *Phys. Rev. D* **2020**, *101*, 056011. [CrossRef]
74. Noronha, J.L.; Shovkovy, I.A. Color-flavor locked superconductor in a magnetic field. *Phys. Rev. D* **2007**, *76*, 105030. [CrossRef]
75. Fukushima, K.; Warringa, H.J. Color Superconducting Matter in a Magnetic Field. *Phys. Rev. Lett.* **2008**, *100*, 032007. [CrossRef]
76. Curin, D.; Ranea-Sandoval, I.F.; Mariani, M.; Orsaria, M.G.; Weber, F. Hybrid Stars with Color Superconducting Cores in an Extended FCM Model. *Universe* **2021**, *7*, 370. [CrossRef]
77. Alford, M.; Braby, M.; Paris, M.; Reddy, S. Hybrid stars that masquerade as neutron stars. *Astrophys. J.* **2005**, *629*, 969. [CrossRef]
78. Alford, M.; Kouvaris, C.; Rajagopal, K. Evaluating the gapless color-flavor locked phase. *Phys. Rev. D* **2005**, *71*. [CrossRef]
79. Alford, M.; Jotwani, P.; Kouvaris, C.; Kundu, J.; Rajagopal, K. Astrophysical implications of gapless color-flavor locked quark matter: A hot water bottle for aging neutron stars. *Phys. Rev. D* **2005**, *71*. [CrossRef]
80. Riley, T.E.; Watts, A.L.; Ray, P.S.; Bogdanov, S.; Guillot, S.; Morsink, S.M.; Bilous, A.V.; Arzoumanian, Z.; Choudhury, D.; Deneva, J.S.; et al. A NICER View of the Massive Pulsar PSR J0740+6620 Informed by Radio Timing and XMM-Newton Spectroscopy. *Astrophys. J.* **2021**, *918*, L27. [CrossRef]
81. Miller, M.C.; Lamb, F.K.; Dittmann, A.J.; Bogdanov, S.; Arzoumanian, Z.; Gendreau, K.C.; Guillot, S.; Ho, W.C.G.; Lattimer, J.M.; Loewenstein, M.; et al. The Radius of PSR J0740+6620 from NICER and XMM-Newton Data. *Astrophys. J. Lett.* **2021**, *918*, L28. [CrossRef]
82. Detweiler, S.; Lindblom, L. On the nonradial pulsations of general relativistic stellar models. *Astrophys. J.* **1985**, *292*, 12–15. [CrossRef]
83. Weber, F. *Pulsars as Astrophysical Laboratories for Nuclear and Particle Physics*; Routledge: London, UK, 2017. [CrossRef]
84. Thorne, K.S.; Campolattaro, A. Non-Radial Pulsation of General-Relativistic Stellar Models. I. Analytic Analysis for L >= 2. *Astrophys. J.* **1967**, *149*, 591. [CrossRef]
85. Sotani, H.; Harada, T. Nonradial oscillations of quark stars. *Phys. Rev. D* **2003**, *68*, 024019. [CrossRef]
86. Benhar, O.; Ferrari, V.; Gualtieri, L.; Marassi, S. Quark matter imprint on gravitational waves from oscillating stars. *Gen. Relativ. Gravit.* **2007**, *39*, 1323–1330. [CrossRef]
87. Flores, C.V.; Lugones, G. Constraining color flavor locked strange stars in the gravitational wave era. *Phys. Rev. C* **2017**, *95*, 025808. [CrossRef]
88. Tonetto, L.; Lugones, G. Discontinuity gravity modes in hybrid stars: Assessing the role of rapid and slow phase conversions. *Phys. Rev. D* **2020**, *101*, 123029. [CrossRef]
89. Rodríguez, M.C.; Ranea-Sandoval, I.F.; Mariani, M.; Orsaria, M.G.; Malfatti, G.; Guilera, O.M. Hybrid stars with sequential phase transitions: The emergence of the g_2 mode. *J. Cosmol. Astropart. Phys.* **2021**, *2021*, 009. [CrossRef]

90. Andersson, N.; Kokkotas, K.D. Towards gravitational wave asteroseismology. *Mon. Not. R. Astron. Soc.* **1998**, *299*, 1059–1068. [CrossRef]
91. Benhar, O.; Ferrari, V.; Gualtieri, L. Gravitational wave asteroseismology reexamined. *Phys. Rev. D* **2004**, *70*, 124015. [CrossRef]
92. Lander, S.K.; Jones, D.I.; Passamonti, A. Oscillations of rotating magnetized neutron stars with purely toroidal magnetic fields. *Mon. Not. R. Astron. Soc.* **2010**, *405*, 318–328. [CrossRef]